Transverse electron momentum distribution of spin orbit wavepackets

A. S. Kheifets* and I. A. Ivanov†
Research School of Physical Sciences, The Australian National University, Canberra ACT 0200, Australia
(Dated: July 7, 2014)

We study the transverse electron momentum distribution (TEMD) of the spin orbit wavepackets launched in a pump-probe sequential double ionization from the valence shell of a noble gas atom. Our calculations, based on an accurate numerical solution of the time-dependent Schrödinger equation (TDSE), reproduce a characteristic cusp of the TEMD which is attributed to the Coulomb singularity. The evolution of the TEMD with the time delay between the pump and probe pulses is shown to be similar to the prediction of the standard tunneling formula (TF), as was observed experimentally for argon by Fechner *et al.* [Phys. Rev. Lett. **112**, 213001 (20014)]. However, TDSE calculations show a clear deviation from the TF and predict a much more complicated structure which cannot be reproduced by the target orbital momentum profile filtered by the tunneling Gaussian. The accuracy of the TF can be improved if the target momentum profile is calculated with the Coulomb waves instead of the plane waves.

PACS numbers: 32.80.Rm 32.80.Fb 42.50.Hz

I. INTRODUCTION

Photoelectron spectroscopy of strong field atomic ionization proved to be a useful tool to study the timing of the ionization process. In the multiphoton regime, the time of the photoelectron release can be mapped onto the photoelectron kinetic energy in attosecond streaking experiments [1]. In the tunneling regime, the timing information can be encoded in the photoelectron momentum distribution in the form of the angular tilt with respect to the vector potential direction of the circularly polarized light at the moment of the wave packet release. This experimental design is popularly known as the attoclock [2]. Similarly, the orthogonally polarized two-color laser fields can be used to obtain the sub-cycle timing of the wave packet release from the momentum vector of emitted electrons [3].

In addition to resolving strong field atomic ionization in time, the photoelectron momentum distribution can be used to interrogate atomic and molecular orbital structure [4]. For the longitudinal momentum distribution $p_\parallel$ along the major axis of the linearly polarized light, the acceleration of the photoelectron in the laser field leads to a significant distortion of the initial momentum distribution [5]. For long times after the laser pulse end, the distribution in this direction is centered at $p_\parallel = E_0/\omega$, where E_0 is the peak laser electric field and ω is the carrier frequency [6]. So the information on the momentum distribution in the target orbital is lost. This is not the case for the transverse, or lateral, momentum $p_\perp$ perpendicular to the polarization plane. The electron motion in this direction is not affected by the laser field and only influenced by the Coulomb interaction with the parent ion. If this interaction is neglected, the transverse electron momentum distribution (TEMD) is expected to be a direct image of the bound-state orbital in the momentum space [6–8]:

$$W(p_\perp) = |\psi_{nlm}(p_\perp)|^2 \exp\Big(-\frac{\sqrt{2I}}{E_0}p_\perp^2\Big) \qquad (1)$$

Here, the momentum profile of the target orbital $|\psi_{nlm}(p_\perp)|^2$ is projected into the continuum by a Gaussian shaped filter

$$F(p_\perp) = \exp\left(-\frac{\sqrt{2I}}{E_0}p_\perp^2\right) \equiv \exp\big(-p_\perp^2/\sigma^2\big) \qquad (2)$$

with an intensity-dependent width σ that arises from the standard tunneling theory [5, 9]. In this Gaussian, I is the ionization potential and E_0 is the peak laser electric field.

Prediction of the tunneling formula (TF) (1) has been tested experimentally. In the experiments employing laser light with linear polarization [10] as well as in the heavy ion impact experiments [11, 12], the Coulomb singularity had a very strong effect which resulted in a sharp cusp-like peak at zero momentum instead of a Gaussian distribution predicted by the TF (1). The Gaussian distribution (1) was observed and measured in the experiment with circular polarization [6]. The Gaussian width σ was shown to be within 15% from predictions of the TF (1). Further improvement could be achieved by using a quantitative tunneling formula (QTF) in which the prefactor is not simply the initial-state momentum-distribution but rather a squared transition amplitude from an initial bound state to a plane-wave state with the kinetic momentum $\boldsymbol{k} + \boldsymbol{A}(t)$ [13].

Wörner and Corkum [8] suggested that the TF (1) can be used to image and control multielectron dynamics by laser-induced tunnel ionization. In the proposed experiment, the pump laser pulse tunnel ionizes the valence np^6 shell of a noble gas atom. The singly charged ion is prepared in a coherent superposition of its two lowest

*Electronic address: A.Kheifets@anu.edu.au
†Electronic address: Igor.Ivanov@anu.edu.au

fine structure levels $np^5\ P_{1/2,\ 3/2}$. Because an atomic p-orbital aligned along the laser field is ionized much more easily than the one with the perpendicular orientation, it is the $m = 0$ hole that is created in the first ionization step. The initially created hole is projected onto a pair of closely spaced spin-orbit $P_{1/2}$ and $P_{3/2}$ doublet. Consequently, the hole population oscillates in time between the $m = 0$ and $|m| = 1$ states [8]

$$\begin{array}{lcl} P_{m=0}(\tau) & = & 5/9 \ + \ 4/9 \times \cos(2\pi\tau/T) \\ P_{|m|=1}(\tau) & = & 4/9 \times [1 - \cos(2\pi\tau/T)] \end{array} \qquad (3)$$

Here $2\pi/T = \Delta E$ is the spin-orbit energy splitting of the $P_{1/2,\ 3/2}$ doublet. This dynamic initial electronic state is subject to further tunneling ionization by the second laser pulse which double ionizes the target atom. In result, the double ionization yield oscillates with the same characteristic period T when studied as a function of the time delay τ between the pump and probe pulses. Similar oscillations is experienced by the TEMD because the momentum profiles of the target orbitals with $m = 0$ and $|m| = 1$ are very different having a peak and a node at $p_\perp = 0$, respectively. In this way, the strong field tunnel ionization can be used to interrogate both the dynamics and electronic structure of the singly charged target state.

Perhaps aware of the Coulomb singularity and the cusp in the TEMD, Wörner and Corkum [8] proposed their Gedanken experiment to be performed with the *circular* polarization. Such an experiment was realized by Fechner et al. [14] on the Ar atom but they used the *linear* polarization in their measurements. As expected, instead of the smooth Gaussian TEMD, they observed the cusp-like momentum profiles both for the neutral Ar and the singly ionized Ar^+. However, when the differential TEMD signal was recorded at a given time delay τ relative to the time averaged TEMD, the cusp at $p_\perp = 0$ was completely removed and the predictions of the TF (1) were perfectly reproduced. Thus, by taking the time differential signal, the Coulomb singularity could be eliminated and the signature of the momentum profile of the target orbital of the singly charge ion could be restored.

In the present work, we perform accurate calculations based on a numerical solution of the time-dependent Schrödinger equation (TDSE) which goes beyond the simple tunneling models and various strong field approximations. Our TDSE calculations with linear polarization reproduce a characteristic cusp of the TEMD. The calculated time differential TEMD is qualitatively similar to predictions of the standard tunneling theory evaluated from the TF (1) and the hole population (3). However, numerical calculations return a much more complicated structure which cannot be reproduced by the simple tunneling theory and related to the target electronic structure. To elucidate the origin of the cusp in the TEMD, we modify the TF (1) by calculating the target momentum profile with the Coulomb waves instead of the plane waves. Such a modification did reproduce the cusp. We also performed an analogous TDSE calculation with the circular polarization which returned a cusp-free TEMD. Reduction of the cusp with elliptically polarized laser light, as the degree of ellipticity grows, was demonstrated in our previous work on the hydrogen atom [15]

The paper is organized as follows. In Sec. II we describe our numerical techniques which we use for the TDSE calculations II A and the TF calculations II B. Results of our TF and TDSE calculations are described in Sec. III A and III B, respectively. The atomic units a.u. are used throughout unless otherwise specified.

II. THEORY

A. TDSE formalism

We solve the TDSE for a target atom in the single active electron (SAE) approximation:

$$i\frac{\partial\Psi(\boldsymbol{r})}{\partial t} = \left(\hat{H}_{\rm atom} + \hat{H}_{\rm int}(t)\right)\Psi(\boldsymbol{r}) \ . \qquad (4)$$

The SAE potential is derived by localization of the Hartree-Fock (HF) potential using the numerical recipe described in [16]. This recipe uses a set of continuous HF orbitals calculated by the computer code [17]. As a test, we compare the energies of the $3p$ state of the Ar^+ ion in the HF and localized potentials which differ by not more than 5%. We find it adequate for the purposes of the present work.

The electromagnetic interaction operator $\hat{H}_{\rm int}(t)$ in Eq. (4) is cast in the velocity form:

$$\hat{H}_{\rm int}(t) = \boldsymbol{A}(t)\cdot\hat{\boldsymbol{p}} \ , \qquad \boldsymbol{A}(t) = -\int_0^t \boldsymbol{E}(\eta)\ d\eta. \qquad (5)$$

We consider below the cases of linearly and circularly polarized driving pulses. We use coordinate system with z-axis taken as the quantization axis. In this coordinate system the electric field of the pulse is given by the expressions:

$$\begin{array}{lcl} \boldsymbol{E}(t) & = & E_0 f(t)\cos\omega t\ \hat{\boldsymbol{z}} \\ \boldsymbol{E}(t) & = & \dfrac{E_0}{\sqrt{2}} f(t)\,(\cos\omega t\ \hat{\boldsymbol{x}} + \sin\omega t\ \hat{\boldsymbol{y}}) \end{array} \qquad (6)$$

for the linear (top) and circular (bottom) polarizations. Here $\hat{\boldsymbol{x}}$, $\hat{\boldsymbol{y}}$, and $\hat{\boldsymbol{z}}$ are unit vectors pointing along the coordinate axes. The pulse envelope is chosen as $f(t) = \sin^2(\pi t/T_1)$, where T_1 is the total pulse duration. In the following, we report calculations with $T_1 = 6$ optical cycles for the linearly polarized driving pulse, and $T_1 = 4$ optical cycles for the circularly polarized one (here optical cycle is $2\pi/\omega$). The base frequency $\omega = 0.057$ a.u., which corresponds to the wavelength $\lambda = 790$ nm. In Eq. (6) $E_0 = 0.12$ a.u., which corresponds to the field intensity of 5×10^{14} W/cm^2 for both linearly and circularly polarized pulses.

To solve the TDSE, we employ the strategy tested in the previous works [18, 19]. The solution of the TDSE is represented as a partial waves series:

$$\Psi(\boldsymbol{r},t) = \sum_{l=0}^{L_{\max}} \sum_{\mu=-l}^{l} f_{l\mu}(r,t) Y_{l\mu}(\theta,\phi). \tag{7}$$

The radial part of the TDSE is discretized on the grid with the stepsize $\delta r = 0.05$ a.u. in a box of the size $R_{\max} = 400$ a.u. for the circularly polarized driving pulse, and $R_{\max} = 600$ for the linearly polarized one. The number of partial waves in Eq. (7) was limited to $L_{\max} = 50$. A series of routine checks [18, 19] was performed to ensure that the calculations were converged with respect to variations of the parameters δr, $R_{\max}$ and $L_{\max}$.

Substitution of the expansion (7) into the TDSE gives us a system of coupled equations for the radial functions $f_{l\mu}(r,t)$, describing evolution of the system in time. To solve this system, we use the matrix iteration method developed in [20]. The ionization amplitudes $a(\boldsymbol{p})$ are obtained by projecting solution of the TDSE at the end of the laser pulse on the set of the ingoing scattering states the target atom.

$$\psi_{\boldsymbol{p}}^{(-)}(\boldsymbol{r}) = \sum_{l\mu} i^l e^{-i\delta_l} Y_{l\mu}^*(\boldsymbol{n_p}) Y_{l\mu}(\boldsymbol{n_r}) R_{kl}(r) \ . \tag{8}$$

Here $\boldsymbol{n_p} = \boldsymbol{p}/p$, and $\boldsymbol{n_r} = \boldsymbol{r}/r$ are unit vectors in the direction of $\boldsymbol{p}$ and $\boldsymbol{r}$, respectively.

The transverse electron momentum distribution, describing probability to detect a photoelectron with a given momentum component $p_\perp$ perpendicular to the polarization plane, is obtained as

$$W(p_\perp) = \int |a(\boldsymbol{p})|^2 \ dp_x \ dp_y \ , \tag{9}$$

for the circularly polarized driving pulse, and:

$$W(p_\perp) = \int |a(\boldsymbol{p})|^2 \ dp_y \ dp_z \ , \tag{10}$$

for the linearly polarized one.

B. Tunneling formula evaluation

1. Target momentum profiles

The TEMD is evaluated using the following procedure. First, the momentum space wave function of the target orbital is calculated

$$\psi_{nlm}(\boldsymbol{p}) = \int d^3r \ \exp(-i\boldsymbol{pr}) \psi_{nlm}(\boldsymbol{r}) \ . \tag{11}$$

The atomic orbital is written as a product of the radial and angular parts $\psi_{nlm} = Y_{lm}(\hat{\boldsymbol{r}}) P_{nl}(r)/r$. By using the partial wave expansion for $\exp(-i\boldsymbol{pr})$ and the orthogonality of the spherical harmonics, we obtain

$$\begin{aligned} |\psi_{nlm}(\boldsymbol{p})|^2 \ &\propto \ \left| Y_{lm}(\hat{\boldsymbol{p}}) \int_0^\infty r dr \, j_l(pr) P_{nl}(r) \right|^2 \\ &\equiv \ |Y_{lm}(\hat{\boldsymbol{p}})|^2 \rho_{nl}(p) \end{aligned} \tag{12}$$

Here the spherically integrated momentum density

$$\rho_{nl}(p) \propto \left| \int_0^\infty r dr \, j_l(pr) P_{nl}(r) \right|^2 \tag{13}$$

is expressed as the squared radial integral with the spherical Bessel function $j_l(pr)$. By using explicit expressions for the spherical harmonics

$$|Y_{10}(\hat{\boldsymbol{p}})|^2 = \frac{3}{4\pi}\frac{p_\parallel^2}{p^2} \ \ , \ \ |Y_{1\pm1}(\hat{\boldsymbol{p}})|^2 = \frac{3}{8\pi}\frac{p_\perp^2}{p^2} \ \ , \ \ p^2 = p_\perp^2 + p_\parallel^2$$

we perform the partial integration to obtain the following momentum profiles:

$$|\psi_{np,m=0}(p_\perp)|^2 \ = \ \frac{3}{4\pi} \int_0^\infty dp_\parallel \frac{p_\parallel^2}{p^2} \rho_{np}(p) \tag{14}$$

$$|\psi_{np,m=\pm1}(p_\perp)|^2 \ = \ \frac{3}{8\pi} p_\perp^2 \int_0^\infty dp_\parallel \frac{1}{p^2} \rho_{np}(p) \to 0 \ \ \text{as} \ \ p_\perp \to 0$$

These profiles are plugged into Eq. (1) to obtain the m-specific TEMD:

$$W_m(p_\perp) = |\psi_{np\,m}(p_\perp)|^2 \exp\left(-\frac{\sqrt{2I_{np}}}{E} p_\perp^2 \right) \tag{15}$$

The target momentum profiles (15) behave differently for small transverse momenta $p_\perp \to 0$. The $m = 0$ profile stays finite whereas $|m = 1|$ one is vanishing. Combined with a rapidly decaying Gaussian factor, this behavior explains why $|W_0(p_\perp)| \gg |W_1(p_\perp)|$.

To elucidate the role of the Coulomb field of the singly or doubly charged parent ion left behind by the photoelectron, we also perform calculations of the momentum profiles (15) using the spherically integrated momentum density in which the spherical Bessel function $\jmath_l(x)$ is substituted by the regular Coulomb function $x^{-1}F_l(\eta, x)$. The Sommerfeld parameter $\eta = -Z^a/p$ is calculated with the asymptotic charge seen by the receding photoelectron: $Z^a = 1$ for Ar^+ and $Z^a = 2$ for Ar^{2+}. In this way, we substitute the plane waves in (11) with the corresponding Coulomb wave. In case of the zero asymptotic charge, the Coulomb function becomes the spherical Bessel function $x^{-1}F_l(\eta = 0, x) = j_l(x)$

and the Coulomb wave becomes the plane wave. The TEMD calculated with the Coulomb function is marked with the c-index $W_m^c(p_\perp)$ to differentiate it from the ordinary TEMD $W_m(p_\perp)$ calculated with the Bessel function.

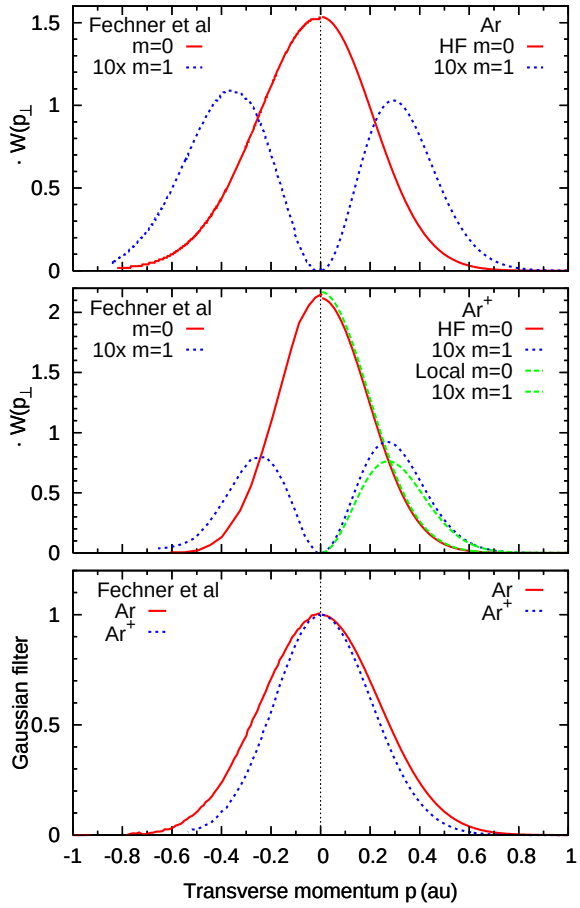

FIG. 1: (Color online) Top panel: The TEMD $W_m(p_\perp)$ of the Ar $3p$ $m = 0$ (solid red line) and $m = 1$ (dotted blue line) states calculated with the HF orbitals (right) and the hydrogenic orbitals [14] (left). $W_{m=1}(p_\perp)$ is multiplied by a factor of 10 for better visibility. Middle panel: same for the Ar^+ ion. The green dashed lines on the right show the TEMD calculated with the orbitals found in the localized potential. Bottom panel: Gaussian filter functions for the field intensity of 5×10^{14} W/cm^2 for the neutral Ar atom (solid red line) and the Ar^+ ion (dotted blue line) in the present calculation (right) and from Ref. [14] (left).

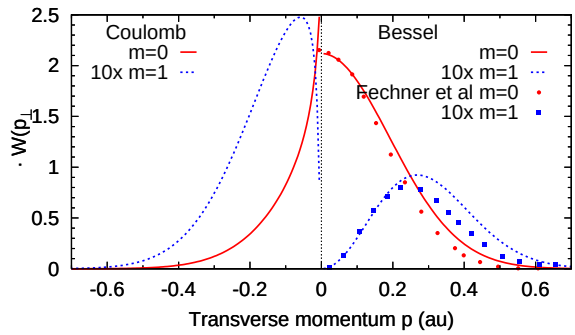

FIG. 2: (Color online) Right: the TEMD $W_m(p_\perp)$ of the Ar^+ ion for the $3p$ states with $m = 0$ (solid red line) and $m = 1$ (dotted blue line). The calculation by Fechner et al. [14] is shown with the colored dots. Right: the TEMD $W^c_m(p_\perp)$ calculated with the Coulomb functions instead of the Bessel functions.

III. RESULTS

A. Tunneling formula calculations

The TEMD $W_m(p_\perp)$ of the $3p$ orbital for the two projections $m = 0$ and $|m| = 1$ are presented in Figure 1 for the neutral Ar atom (top panel) and the singly ionized Ar^+ ion (middle panel). The $m = 1$ TEMD is multiplied by a factor of 10 to be visible on the same scale. In the same figure, we make a comparison with the analogous calculation of Fechner et al. [14] who employed hydrogenic orbitals with a set of effective charges. Both calculations are shown as mirror images on the opposite halves of the transverse momentum scale. On the bottom panel of the figure, we show the Gaussian filters (2) in both calculations evaluated with the same field intensity of 5×10^{14} W/cm^2. The presently calculated Gaussians appear to be slightly wider, most probably because of the difference in ionization potentials with Ref. [14].

In Figure 2 we display an analogous set of TEMD $W^c_m(p_\perp)$ calculated with the Coulomb functions instead of the Bessel functions. The transformation of the TEMD is radical. For $m = 0$, a smooth Gaussian peak at $p_\perp = 0$ is replaced by a sharp cusp. For $m = 1$, the geometrical node at $p_\perp = 0$ remains in place but it follows by steep rise of the TEMD which turns into a sharp fall. This behavior is the consequence of the Coulomb singularity. In a special case of $p \to 0$ and $r \to 0$ when $\eta = Z/p < 0$ and is large [21],

$$F_l(\eta, pr) = \sqrt{\frac{\pi}{2|\eta|}} \frac{(2pr|\eta|)^{l+1}}{(2l+1)!} \propto p^{-1/2}$$

which is singular for all l. This singularity is smoothed somewhat a factorial $(2l + 1)!$ for large l. This inverse square root singularity is imprinted in $W^c_{m=0}(p_\perp \to 0)$ and only partially cured by the geometrical node in $W^c_{|m|=1}(p_\perp \to 0)$.

1. *Time differential TEMD*

The electron occupation numbers in the Ar^+ ion are related to the hole occupation numbers (3) as:

$$\begin{aligned} D_{m=0}(\tau) &= 2 - P_{m=0}(\tau) &&= 13/9 - 4/9\cos(2\pi\tau/T) \\ D_{|m|=1}(\tau) &= 4 - P_{|m|=1}(\tau) &&= 32/9 + 4/9\cos(2\pi\tau/T) \end{aligned} \tag{16}$$

These occupation numbers can be used to calculate the time-specific TEMD summed over all the target electrons:

$$W(p_\perp, \tau) = \sum_{|m|=0,1} W_m(p_\perp) D_m(\tau) \tag{17}$$

The time-averaged TEMD is evaluated as

$$W(p_\perp) = \int_0^T W(p_\perp, \tau) d\tau \tag{18}$$

Both the time-specific and time averaged TEMD are normalized

$$\overline{W}(p_\perp, \tau) = A^{-1} W(p_\perp, \tau) \quad , \quad A = \int_0^\infty W(p_\perp, \tau) p_\perp dp_\perp$$

$$\overline{W}(p_\perp) = A^{-1} W(p_\perp) \quad , \quad A = \int_0^\infty W(p_\perp) p_\perp dp_\perp$$

and the time-differential TEMD is evaluated as

$$\Delta W(p_\perp, \tau) = \left[\overline{W}(p_\perp, \tau) - \overline{W}(p_\perp)\right] p_\perp \ , \tag{19}$$

where

$$\overline{W}(p_\perp) = \frac{13W_0(p_\perp) + 32W_1(p_\perp)}{13|W_0| + 32|W_1|} \tag{20}$$

$$\overline{W}(p_\perp, \tau = \frac{nT}{2}) = \frac{17W_0(p_\perp) + 28W_1(p_\perp)}{17|W_0| + 28|W_1|}$$

$$\overline{W}(p_\perp, \tau = nT) = \frac{W_0(p_\perp) + 4W_1(p_\perp)}{|W_0| + 4|W_1|}$$

Here $|W_m| = \int_0^\infty W_m(p_\perp) p_\perp dp_\perp$

The time-differential TEMD is shown in Figure 3 for the time delays equal to an integer $\tau = nT$ (top) and a half integer $\tau = nT/2$ (bottom) number of periods of the spin-orbit oscillations together with the analogous set of data from Fechner et al. [14]. The present Bessel function calculations both with the HF and localized orbitals are very similar to hydrogenic orbital calculation in Ref. [14]. The Coulomb function calculation with the HF orbital is qualitatively similar but visually different. Even though the Coulomb singularity is not seen directly in the time differential TEMD, it makes it contracted in the transverse momentum scale and the crossing point is moved closer to the origin.

B. TDSE calculations

Solution of the TDSE (4) is found by time propagation of the initial state of the target. To describe the dynamic initial state of the Ar^+ ion with the electron population given by Eq. (16) we employ the density matrix formalism. A completely incoherent density matrix representing the initial ensemble of the Ar^+ ions is given by the following expression:

$$\hat{\rho}_1 = \frac{1}{2\pi} \int_0^{2\pi} |\Psi_\phi\rangle\langle\Psi_\phi| \ d\phi \ . \tag{21}$$

Here $|\Psi_\phi\rangle$ is a coherent superposition of the normalized $3p$ states with the $m = 0$ and $m = 1$ projections

$$|\Psi_\phi\rangle = \sqrt{p_{m=0}(\tau)}\Psi_{m=0} + e^{i\phi}\sqrt{p_{|m|=1}(\tau)}\Psi_{|m|=1} \ , \tag{22}$$

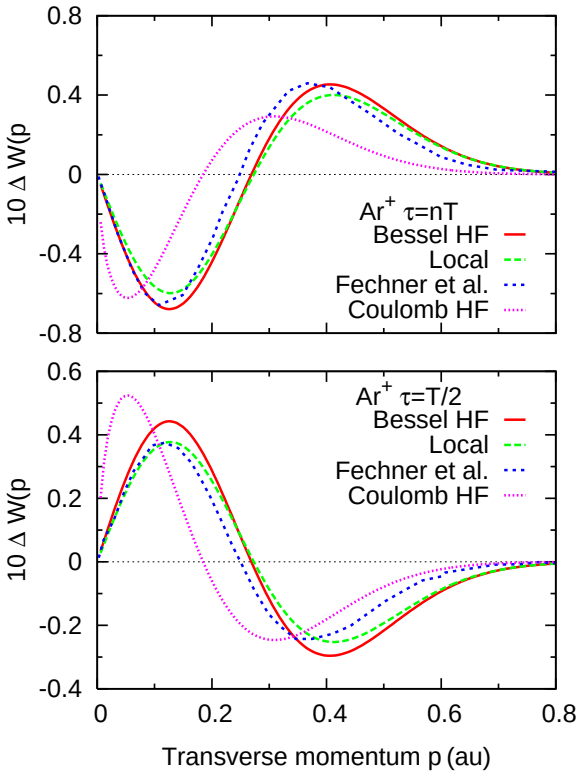

FIG. 3: The time differential TEMD $\Delta W(p_\perp, \tau)$ for the Ar^+ ion calculated at the time delays equal to an integer $\tau = nT$ (top) and half integer $\tau = nT/2$ (bottom) periods of the spin-orbit oscillation. The Bessel function calculations with the HF (red solid lines) and localized (green dashed lines) orbitals are compared with calculations of Fechner et al. [14] with hydrogenic orbitals (blue dotted lines). The dotted puprle line shows the Coulomb function calculation with the HF orbital.

The normalization coefficients are related to the occupation numbers (16) as $p_m(\tau) = D_m(\tau)/5$. An arbitrary phase ϕ in Eq. (22) is averaged over in Eq. (21). Using Eq. (22) to evaluate the integral in Eq. (21) density matrix $\hat{\rho}_1$ can be more conveniently represented as:

$$\hat{\rho}_1 = \sum_{|m|=0,1} p_m |\Psi_m\rangle\langle\Psi_m| \tag{23}$$

TDSE calculations with the density matrix (21) are thus equivalent to two independent calculations from the initial $3p$ states of the Ar^+ ion with $m = 0$ and $m = 1$ projections. Using the procedure described by Eq. (9) (linear polarization) or Eq. (10) (circular polarization) we obtain the TEMD $W_{m=0}(p_\perp)$ and $W_{|m|=1}(p_\perp)$. The time-specific TEMD corresponding to a particular value of delay τ is obtained as an incoherent sum

$$W(p_\perp, \tau) = \sum_{|m|=0,1} p_m(\tau) W_m(p_\perp) \tag{24}$$

The phase averaging in Eq. (21) is based on the assumption that all the relative phases ϕ are equally probable. As an additional test, we performed a separate set of calculations with the density matrix favoring one particular

value of the relative phase ϕ:

$$\hat{\rho}_2 = |\Psi_0\rangle\langle\Psi_0|, \tag{25}$$

where $|\Psi_0\rangle$ is the state (22) with $\phi = 0$. The density matrix (25) describes a pure state which is a coherent superposition of the $3p_m$ states of the Ar^+ with $m = 0$ and $|m| = 1$. We shall see below that results of the calculations using the incoherent density matrix (21) and the coherent matrix (25) are quite similar. This indicates that our results are not very sensitive to the fine details of the preparation of the ensemble of Ar^+ ions in the experiment.

All the TDSE calculations shown below were performed for the values of the time delay between the pump and probe pulses τ ranging from 0 to $0.9T$ with an increment of $0.1T$, $T = 2\pi/\Delta E$ being the period of the spin-orbit oscillations. Except for the data shown in Figure 5 which were calculated both with the density matrices (21) and (25), the incoherent density matrix (21) was used.

1. *Linear polarization*

In Figure 4 we present the results of our TDSE calculation for the time-averaged TEMD of the Ar^+ ion in comparison with experimental data [14]. Similar to the experiment, the calculated results are binned into the intervals of the transverse momentum with the width of $\Delta p_\perp = 0.02$ a.u. Both the calculation and the experiment demonstrate a cusp-like peak at $p_\perp = 0$. Away from this peak, the TEMD is falling rather quickly. A similar monotonous fall away from the cusp is seen in the TF calculation with the Coulomb function and the HF orbital also shown in the figure. When superimposed on the binned experimental data, a close resemblance can be seen. In the TDSE calculation the fall away from the cusp is initially very steep but then flattens with a shoulder-like structure. This structure is seen more clearly for the time-differential TEMD shown in Figure 5 for the time delays equal to integer $\tau = nT$ (top) and half integer $\tau = nT/2$ (bottom) periods of the spin-orbit oscillation. Here we make a comparison of the TDSE calculations with an incoherent and the coherent dynamic initial state. The difference between the two calculations is rather small and can only be seen in fine details.

Fechner et al. [14] concluded that their time-differential TEMD reproduces the TF with hydrogenic orbitals. This is indeed seen in Figure 6 where we make a comparison of the experimental data with the TF and TDSE calculations. The TDSE calculation is visibly different from the TF with the the localized orbitals. For an integer number of oscillations (top panel), the TDSE calculation is rather close to the TF calculated with the Coulomb function and the HF orbital. For a half-integer number of oscillations (bottom panel), this similarity is lost. Unfortunately, the experimental error bars are too large to discriminate between different calculations. On the top panel, however, the TF with the hydrogenic orbitals is the closest to the experiment.

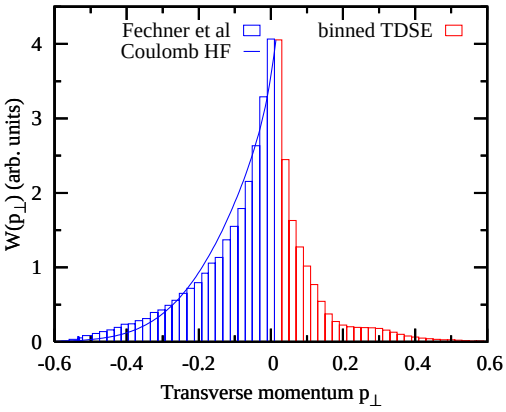

FIG. 4: The time-averaged TEMD of the Ar^+ ion. Right: TDSE calculation. Left: experiment by Fechner et al. [14] and the TF calculation with the Coulomb function and the HF orbital (blue solid line).

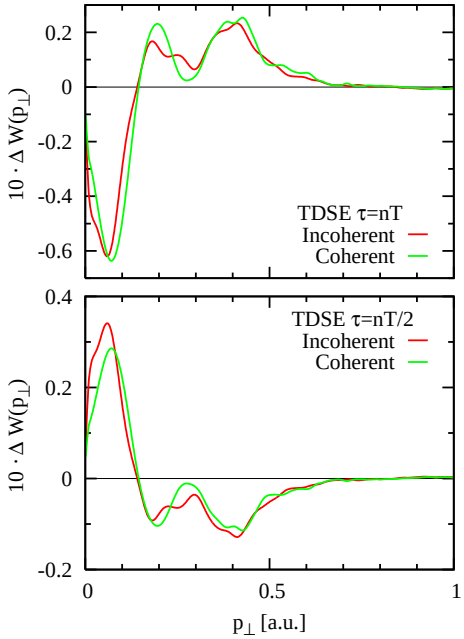

FIG. 5: Top panel: the time differential TEMD $\Delta\overline{W}(p_\perp, \tau)$ for the Ar^+ ion calculated at the time delays equal to an integer number of periods of the spin-orbit oscillation. Incoherent density matrix (21) (red solid line), coherent density matrix (25) (green dash). Bottom panel: same for time delays equal to a half integer number of periods of the spin-orbit oscillation.

2. *Circular polarization*

The circular polarization computations are much more demanding in comparison to the linear polarization case because of a slower convergence of the expansion (7).

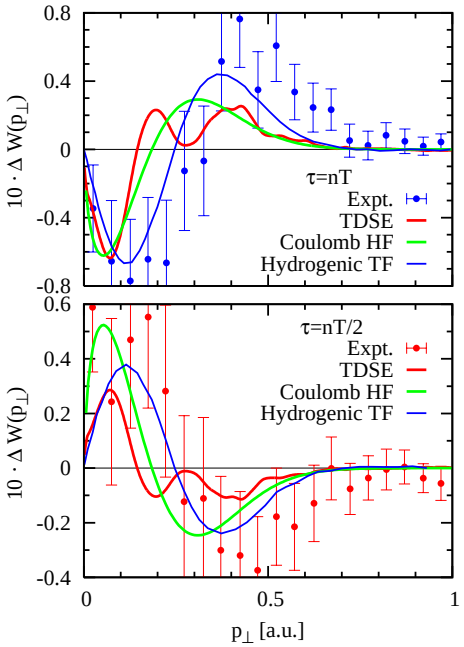

FIG. 6: The time differential TEMD $\Delta W(p_\perp, \tau)$ for the Ar^+ ion calculated at various time delays equal to an integer $\tau = nT$ (top panel) and a half integer $\tau = nT/2$ (bottom panel) periods of the spin-orbit oscillation. TDSE calculations (red solid line) are compared with the TF calculations with the hydrogenic orbital (blue solid lines), the TF calculations with the Coulomb waves and the HF orbitals (green lines) and experiment of Fechner et al. [14] (error bars)

Physically, absorption of a photon from the circularly polarized light increases the magnetic quantum number of the target by one unit. It is required at least 20 photons to ionize the Ar^+ ion by the laser light of 800 nm. This means that the number of partial waves to be retained in the expansion (7) should be at least that large. In fact, a good numerical convergence is achieved at a considerably larger number of 50 partial waves. The reward for this rather demanding calculation is substantial, however. The TEMD for the case of circular polarization exhibits much nicer properties. Most importantly, there is no cusp in the TEMD, in agreement with the experimental observation [6]. Another difference between linear and circular polarization cases, is that ionization probabilities from $m = 0$ and $m = 1$ cases may have comparable magnitudes [19] while for the linear polarization case ionization from the $m = 0$ state is by far dominant. This can be understood from the following properties of the spherical harmonics [22]

$$Y_{l,|m|=l} \propto (p_\perp/p)^l \ , \ Y_{l,|m|=l-1} \propto (p_\perp/p)^{l-1} \ , \ p^2 = p_\perp^2 + p_\parallel^2$$

The linear polarization case permits a small $l = 1$ which enters the TF (1) and clearly favors the $m = 0$ projection over the $|m| = 1$ projection. In the circular polarization case, l should be very large and the difference between the $m = 0$ and $|m| = 1$ projections is not so dramatic as both have a node as $p_\perp \to 0$.

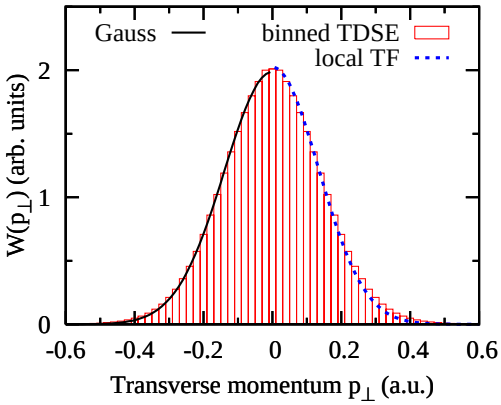

FIG. 7: The time-averaged TEMD of the Ar^+ ion for circularly polarized driving pulse. Binned TDSE calculation is shown with boxes. The TF calculation with the localized $3p$ orbital of the Ar^+ ion is shown on the right by the blue dotted line. The Gaussian fit $\exp(-p_\perp^2/\sigma^2)$ is shown by the black solid line on the left.

The time-averaged TEMD from the TDSE calculation is shown in Figure 7. The TEMD is Gaussian as predicted by the TF (1). The Gaussian width parameter $\sigma = 0.2$ a.u. This can be compared with the analogous parameter $\sigma = 0.25$ a.u. for the neutral Ar atom at the field intensity of 5×10^{14} W/cm^2 reported by Arissian et al. [6].

The time-differential TEMD is shown in Figure 8 for the time delay equal to an integer (top) and a half-integer (bottom) number of the spin-orbit oscillations. We note that the phase of the oscillations of the TEMD is *opposite* as compared to the prediction of the TF (1) and the linear polarization case shown in Figure 5 and Figure 6. We also note that the TEMD is smooth and shows no fine structure visible in the case of linear polarization.

IV. CONCLUSION

We performed a study of the the transverse electron momentum distribution (TEMD) of the coherent superposition of spin orbit wavepackets launched in a sequential pump-probe double ionization from the valence shell of a noble gas atom. In agreement with the experimental results [10] our TDSE calculation for a linearly polarized driving pulse shows a characteristic cusp of the TEMD which is attributed to the Coulomb singularity. The evolution of the TEMD with the time delay between the pump and probe pulses is shown to be similar to the prediction of the standard tunneling theory based on the SFA, as was observed experimentally for argon by Fechner et al. [14]. The agreement between the simple tunneling formula (TF) and the TDSE calculations is, however, qualitative at best. This largest disagreement is pronounced in a Gaussian TEMD predicted by the TF which is missing altogether the cusp structure

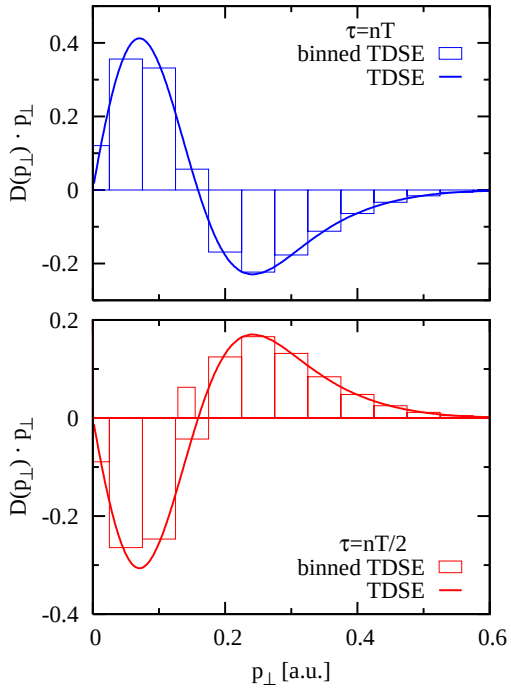

FIG. 8: Color online. The time differential TEMD $\Delta\overline{W}(p_\perp, \tau)$ for the Ar^+ ion calculated at time delays equal to integer $\tau = nT$ (top) and half integer $\tau = nT/2$ (bottom) periods of the spin-orbit oscillation. Solid (red) line: TDSE calculation, dashed (green) boxes: TDSE calculation binned into $\Delta p_\perp = 0.05$ a.u. intervals of transverse momentum for better comparison with experiment.

in the TEMD at $p_\perp \to 0$. The actual TEMD is more complicated than a simple Gaussian, and it cannot be reproduced by the target orbital momentum profile filtered by the tunneling theory Gaussian. The TF can be improved somewhat if the Coulomb functions are used instead of the spherical Bessel functions when the momentum profile of the target orbital is calculated. Thus modified TF does produce the cusp.

For a circularly polarized driving pulse, the time-averaged TEMD is cusp-free and can be described well by a simple TF (1). However, the time-differential TDSE is very different from the TF predictions, the phase of the oscillations being opposite to this predictions for the linear polarization case. This is so because absorption of many photons from circularly polarized light can only be accommodated by large orbital momenta which are not incorporated in the TF.

Acknowledgment

We thank Thomas Pfeifer and Lutz Fechner for many stimulating discussions. The authors acknowledge support of the Australian Research Council in the form of the Discovery grant DP120101805. Resources of the National Computational Infrastructure (NCI) Facility were employed.

[1] M. Schultze *et al*, *Delay in Photoemission*, Science **328**(5986), 1658 (2010).

[2] P. Eckle *et al*, *Attosecond Ionization and Tunneling Delay Time Measurements in Helium*, Science **322**(5907), 1525 (2008).

[3] L. Zhang, X. Xie, S. Roither, D. Kartashov, Y. Wang, C. Wang, M. Schöffler, D. Shafir, P. Corkum, A. Baltuška, et al., *Laser-sub-cycle two-dimensional electron momentum mapping using orthogonal two-color fields*, Phys. Rev. Lett. p. submitted (2014), arXiv 1404.5742.

[4] M. Meckel, D. Comtois, D. Zeidler, A. Staudte, D. Pavicić., H. C. Bandulet, H. Pépin, J. C. Kieffer, R. Dörner, D. M. Villeneuve, et al., *Laser-induced electron tunneling and diffraction*, Science **320**(5882), 1478 (2008).

[5] N. B. Delone and V. P. Krainov, *Energy and angular electron spectra for the tunnel ionization of atoms by strong low-frequency radiation*, J. Opt. Soc. Am. B **8**(6), 1207 (1991).

[6] L. Arissian, C. Smeenk, F. Turner, C. Trallero, A. V. Sokolov, D. M. Villeneuve, A. Staudte, and P. B. Corkum, *Direct test of laser tunneling with electron momentum imaging*, Phys. Rev. Lett. **105**, 133002 (2010).

[7] M. Spanner, O. Smirnova, P. B. Corkum, and M. Y. Ivanov, *Reading diffraction images in strong field ionization of diatomic molecules*, J. Phys. B **37**(12), L243 (2004).

[8] H. J. Wörner and P. B. Corkum, *Imaging and controlling multielectron dynamics by laser-induced tunnel ionization*, J. Phys. B **44**(4), 041001 (2011).

[9] N. B. Delone and V. P. Krainov, *Tunneling and barrier-suppression ionization of atoms and ions in a laser radiation field*, Physics-Uspekhi **41**(5), 469 (1998).

[10] A. Rudenko, K. Zrost, T. Ergler, A. B. Voitkiv, B. Najjari, V. L. B. de Jesus, B. Feuerstein, C. D. Schr.ter, R. Moshammer, and J. Ullrich, *Coulomb singularity in the transverse momentum distribution for strong-field single ionization*, J. Phys. B **38**(11), L191 (2005).

[11] R. Moshammer, B. Feuerstein, W. Schmitt, A. Dorn, C. D. Schröter, J. Ullrich, H. Rottke, C. Trump, M. Wittmann, G. Korn, et al., *Momentum distributions of nen+ ions created by an intense ultrashort laser pulse*, Phys. Rev. Lett. **84**, 447 (2000).

[12] A. B. Voitkiv and B. Najjari, *Ionization of helium by relativistic highly charged ions within the symmetric eikonal approximation*, J. Phys. B **37**(24), 4831 (2004).

[13] I. Dreissigacker and M. Lein, *Quantitative theory for the lateral momentum distribution after strong-field ionization*, Chem. Phys. **414**(0), 69 (2013).

[14] L. Fechner, N. Camus, J. Ullrich, T. Pfeifer, and R. Moshammer, *Strong-field tunneling from a coherent superposition of electronic states*, Phys. Rev. Lett. **112**, 213001 (2014).

[15] I. A. Ivanov, *Evolution of the transverse electron momentum distribution with varying laser pulse ellipticity* p. submitted (2014).

[16] G. Wendin and A. F. Starace, *Perturbation theory in a strong-interaction regime with application to 4d-subshell spectra of Ba and La* **11**(24), 4119 (1978).

[17] L. V. Chernysheva, N. A. Cherepkov, and V. Radojevic, *SCFHF program*, Comp. Phys. Comm. **11**, 57 (1976).

[18] I. A. Ivanov, *Time delay in strong-field photoionization of a hydrogen atom*, Phys. Rev. A **83**(2), 023421 (2011).

[19] I. A. Ivanov and A. S. Kheifets, *Time delay in atomic photoionization with circularly polarized light*, Phys. Rev. A **87**, 033407 (2013).

[20] M. Nurhuda and F. H. M. Faisal, *Numerical solution of time-dependent schrödinger equation for multiphoton processes: A matrix iterative method*, Phys. Rev. A **60**(4), 3125 (1999).

[21] H. Friedrich, *Theoretical Atomic Physics* (Springer Verlag, Berlin Heidelberg, 2006).

[22] D. A. Varshalovich, A. N. Moskalev, and V. K. Khersonskii, *Quantum theory of angular momentum* (World Scientific, Singapore, 1988).